Dalton Transactions

Accepted Manuscript

ROYAL SOCIETY OF CHEMISTRY

www.rsc.org/dalton

Journal Name

ARTICLE

Reduced graphene oxide anchored $Cu(OH)_2$ as high performance electrochemical supercapacitor

Received 00th January 20xx,
Accepted 00th January 20xx

DOI: 10.1039/x0xx00000x

www.rsc.org/

Atin Pramanik, Sandipan Maiti and Sourindra Mahanty*

Developing new materials for electrochemical supercapacitors with higher energy density has gained tremendous recent impetus in the context of effective utilization of renewable energy. Herein, we report a simple one-pot synthesis of bundled nanorods of $Cu(OH)_2$ embedded in a matrix of reduced graphene oxide ($Cu(OH)_2$@RGO) under mild hydrothermal conditions of 80°C for 1 h. The synthesized material shows a high BET surface area of 78.7 $m^2 g^{-1}$ and a mesoporous nature with a broad pore-size distribution consisting of structural pores as well as inter-particle pores. Raman spectroscopy suggests an intimate interaction between $Cu(OH)_2$ and reduced graphene oxide (RGO) creating more defects by destruction of sp^2 domains which would help the defect-assisted charge transport during electrochemical processes. When investigated as an electrochemical supercapacitor, $Cu(OH)_2$@RGO shows a high capacitance of 602 Fg^{-1} at 0.2 Ag^{-1} in 1 M KOH in three-electrode cell configuration. Detailed electrochemical studies indicate that the faradic processes are diffusion controlled and follow a quasi-reversible kinetics. Further, a two-electrode symmetric cell shows good energy density and power density (84.5 $WhKg^{-1}$ at 0.55 $KWKg^{-1}$ and 20.5 $WhKg^{-1}$ at 5.5 $KWKg^{-1}$) characteristics demonstrating superior application potential of this common low-cost transition metal hydroxide for high performance energy storage devices.

1. Introduction

Energy storage devices are increasingly becoming important for the success of renewable energy utilization by bridging the gap between supply and demand. In this respect, electrochemical supercapacitors are in the forefront due to their intrinsically high conversion efficiency and compatibility with energy generated form solar, wind, nuclear etc., in addition to the unique advantages that include a simple principle, high dynamics of charge propagation, pulsed power supply and long steady cycle life.[1-3] Electrical charge can be stored in a supercapacitor through two basic mechanisms, acting either separately or in combination: (i) formation of an electrical double layer (non-faradic) in the electrode-electrolyte interface and (ii) charge transfer (faradic) across the electrode-electrolyte interface. The physico-chemical properties of the electro-active material are the most important factors governing the electrochemical performance. Carbonaceous materials,[3-5] such as activated carbon, carbon nanotube,[6-7] carbon nanofiber,[8-9] graphene[10-11] etc, have been utilized in electrical double layer capacitor (EDLC) due to their high surface to volume ratio, outstanding electrical conductivity and excellent mechanical/electrochemical stability. Still, the presently available commercial EDLCs can offer energy densities in the range of only 5-10 $WhKg^{-1}$. On the other hand, by exploiting the pseudocapacitive properties of conducting polymers[12–13] and transition metal oxides/hydroxides,[14-19] energy densities several times higher than EDLC could be realized (10-200 $WhKg^{-1}$). Most of the transition metal oxides are wide band gap semiconductors or even insulators.[20-21] Therefore, though they exhibit high specific capacitance, their intrinsic poor electronic conductivity limits the power density, thus, compromising the most advantageous characteristic of a supercapacitor. Conducting polymers are inexpensive and flexible, but offer a relatively lower capacitance <100 Fg^{-1} and suffer from chemical instability in the electrolytes resulting in poor cycle life.[20] Recently, transition metal hydroxides such as $Co(OH)_2$, $Ni(OH)_2$ and $Cu(OH)_2$ have emerged as attractive alternatives to the corresponding oxide counterparts on account of their layered structure with large interlayer spacing and well-defined electrochemical redox activity.[22-26] However, most of the studies so far are focused on $Co(OH)_2$[22-23] and $Ni(OH)_2$[24-25] whereas, $Cu(OH)_2$[26] is relatively less explored despite being known to have a fast Cu(II)/Cu(III) redox couple. Recently, a

Fuel Cell & Battery Division, CSIR-Central Glass & Ceramic Research Institute, Kolkata 700032 and CSIR-Network Institutes for Solar Energy (NISE), New Delhi India.
Email: mahanty@cgcri.res.in; s_mahanty@hotmail.com
Tel: +91-33-2322 3495 Fax: +91-33-2473 0957.
† Electronic Supplementary Information (ESI) available: X-ray diffractogram of graphene oxide (GO) and variation of specific capacitance with increasing current density for symmetric cell.

composite electrode, Mn:CuO/$Cu(OH)_2$, showed a capacitance of 600 Fg^{-1} at 5 mVs^{-1} scan rate using 1 M Na_2SO_4 as electrolyte.[2] Except for one report where a low capacitance of 120 Fg^{-1} was observed,[26] there is no work on the supercapacitive properties of $Cu(OH)_2$ in the pristine form. This may be due to the fact that pristine $Cu(OH)_2$ suffers from poor cyclability and low capacity, which are mainly caused by their low conductivity and large volume change during charge/discharge cycles.[27-31] In recent years, it has been demonstrated that developing carbon–inorganic composite could be an effective strategy to improve the electrochemical performance.[12, 32] In this respect, graphene, an intriguing two-dimensional carbon material, with outstanding electrical conductivity and the ability to promote the electron transfer reactions has attracted considerable attention for supercapacitor applications. It is expected that a graphene or graphene-like RGO embedded $Cu(OH)_2$ could offer much improved performance through complete utilization of the fast Cu(II)/Cu(III) redox couple by effective charge transfer through the graphene network. Additionally, such composite can promote the electrical double layer capacitance and accommodate a large amount of superficial electroactive species to participate in faradaic redox reactions. Furthermore, any associated volume change could also be mitigated by graphene/RGO serving as a buffering matrix. However, until now, to the best of our knowledge, no report is available on the performance of $Cu(OH)_2$@RGO as an electrochemical supercapacitor. Chemical reduction of graphene oxide (GO) is considered to be the most economical approach for preparing graphene *in-situ*. Being hydrophilic and containing a large number of oxygen containing groups such as OH, COOH etc, GO is readily dispersed in water producing single layers. Therefore, in the present work, we have adopted a one-pot synthesis strategy to prepare $Cu(OH)_2$@RGO by a simple low-temperature hydrothermal process and investigated its performance as electrochemical supercapacitor. We show here that the synthesized composite, when studied in three-electrode cell configuration, exhibits a specific capacitance as high as 602 Fg^{-1} at a constant current density of 0.2 Ag^{-1} in 1 M KOH electrolyte together with good rate performance and cycling stability. Further to demonstrate its practical applicability, following the best practice method,[23, 33-35] symmetric cells in two-electrode configuration have been studied which show a high energy density of 84.5 Wh Kg^{-1} and excellent cycling stability.

2. Experimental

2.1 Chemicals

The chemicals used were in the as-received form, without further purification. In all experiments, ultrapure water obtained from a three-stage Millipore Mill-Q (Merck, Germany) purification system, was used. The following chemicals were used for synthesis: graphite powder (99.99%, Merck, Germany), copper nitrate nonahydrate [$Cu(NO_3)_2.9H_2O$] (99%, Merck, Germany), $KMnO_4$ (97%, Merck, Germany), 25% ammonia (99%, RANKEM, India), NaOH (≥98%, Merck, Germany), H_2SO_4, HCl, H_2O_2 and $NaNO_3$ (≥99%, Merck, Germany).

2.2 Synthesis of graphene oxide

The graphene oxide (GO) was prepared following an improved modified Hummer method.[36-37] In a typical experiment, graphite powder (5.0 g) was thoroughly mixed in 150 ml of concentrated H_2SO_4 keeping the solution in an ice bath (0-5°C) to which 2.5 g of $NaNO_3$ was added under vigorous stirring condition. After ~3 h, $KMnO_4$ (20.0 g) was slowly added to the above mixture maintaining the solution temperature not exceeding 35°C. After ~1 h, warm H_2O (250.0 ml) was added slowly raising the mixture temperature to ~95°C and maintained for ~30 min. Thereafter, the temperature of the solution was lowered to ~30°C by putting into ice bath. Warm H_2O (500.0 ml) and 30% H_2O_2 were added into it gradually till the color of the solution turned from purple-green to bright yellow. After stirring for 1 h, the reaction was ended by cooling to room temperature and the colorless supernatant was removed by centrifugation at 4000 rpm for 15 min. The precipitate was then washed several times with deionized water, 30% HCl and ethanol successively. After vacuum drying at 50°C for ~12 h, the resulting brown solid (GO) was collected and stored for further experiments.

2.3 Synthesis of $Cu(OH)_2$@RGO

A schematic of the synthesis strategy adopted in the present study is shown in Scheme-1. At first, 400 mg of the synthesized graphene oxide (GO) powder was mixed with 200 ml of deionized water in the ratio of 2:1 (wt: vol) of GO: H_2O. Then the mixture was ultrasonicated for 1 h to disperse the GO properly in deionized water. After that, the brown dispersion was subjected to 20 min of centrifugation at 4000 rpm to remove any extra aggregates. A homogeneously dispersed graphene oxide suspension was obtained.

The synthesis of reduced graphene oxide anchored $Cu(OH)_2$ [$Cu(OH)_2$@RGO] was carried out as follows. In a typical procedure, 2.41 g of $Cu(NO_3)_2.9H_2O$ was dissolved into 200 ml of GO suspension under stirring condition. Then 6.0 ml of 25%

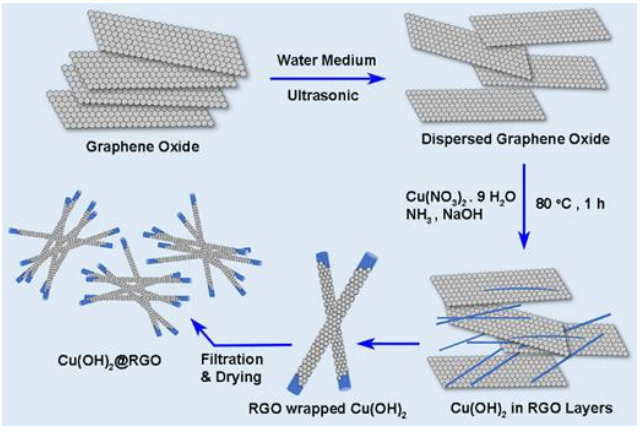

Scheme-1 A schematic of the wet-chemistry strategy for synthesis of $Cu(OH)_2$@RGO composite

ammonia solution added slowly, following which 0.1 M NaOH were added into the above solution under vigorous agitation. The solution was then transferred into a beaker and heated at 80°C for 1 h. After cooling to room temperature, the product was centrifuged and washed several times with deionized water to maintain pH of the product to 7.0 and then, with acetone. Finally, the resulting $Cu(OH)_2$@RGO composite was dried in a vacuum oven at 80°C for 12 h.

For comparison of electrochemical performance, $Cu(OH)_2$ was also synthesized following the same procedure except for using the GO suspension.[38]

2.4 Material characterization

X-ray diffraction of the powder samples was carried out in the 2θ range 10°-80° at a scanning rate of 2° min^{-1} by an X-ray diffractometer (Philips X'Pert, the Netherlands) with a Cu-Kα radiation at 40 KV and 40 mA. Fourier transformed infra-red (FTIR) spectra were recorded by a BOMEN infrared spectrophotometer in transmission mode in the wave number range 4000-400 cm^{-1}. Raman spectroscopy was carried out by Renishaw In Via Reflex micro Raman spectrometer with excitation of argon ion laser (514 nm). A ZEISS Supra 35 (Germany) field emission scanning electron microscope (FESEM) and a 300 kV Tecnai G^2 30ST (FEI) transmission electron microscope were used for observation of the microstructure and morphology of the synthesized powders. A Quantachrome (USA) Autosorb surface analyzer was used to carry out BET surface area measurements at 77.3 K. Thermogravimetric analysis (TGA) was carried out under argon flow at a heating rate of 10 °C min^{-1} using Simultaneous Thermal Analyzer (STA449F, Netzsch, Germany).

2.5 Electrochemical measurements

For fabrication of the working electrodes, a homogeneous slurry was prepared by thoroughly mixing $Cu(OH)_2$@RGO powder with SuperP carbon and polytetrafluoroethylene (PTFE) binder in 80:10:10 weight ratio. The slurry was then casted onto nickel foams of dimension 1.5 cm × 1.5 cm to form the electrodes. The electrodes were then dried at 100°C ~4 h in a vacuum oven to evaporate residual solvents. Mass loading of the active material in the electrodes was between 2.8 and 3.0 mg cm^{-2}. Prior to the electrochemical tests, the electrodes were soaked in 1 M KOH solution for 6 h for proper wetting. The electrochemical experiments were performed both in three-electrode and in two-electrode configurations. In three-electrode set-up, Ag/AgCl (3 M KCl) and Pt mesh (2 cm x 2 cm) were used as the reference and the counter electrode respectively. Two electrode symmetric supercapacitor pouch cells were assembled using two $Cu(OH)_2$@RGO electrodes separated by a Celgard 2300 membrane (thickness, 20 µm). 1 M KOH was used as the electrolyte in all cells. Cyclic voltammetry (CV), galvanostatic charge-discharge and electrochemical impedance spectroscopy (EIS) measurements were conducted using a Galvanostat-Potentiostat (PGSTAT 300N, Autolab, the Netherlands). CVs were measured between 0.0 V to 0.47 V for three-electrode cells and between -0.9 to +0.9 V for two-electrode cells at different scan rates (2 - 100 mVs^{-1}). Galvanostatic charge-discharge measurements were performed at current densities (0.2 - 10 Ag^{-1}) in the same respective potential windows. EIS measurements were carried out at open circuit potential in the frequency range of 0.1 Hz - 1.0 MHz with AC amplitude of 10 mV. The impedance data were fitted to an equivalent circuit model using NOVA 1.9 software.

3. Results and discussion

3.1 Structure and morphology

Formation of $Cu(OH)_2$@RGO composite structure and the phase purity were first examined by X-ray diffraction. The observed peaks in the diffractogram, shown in Fig.1a, correspond to the characteristic reflections of $Cu(OH)_2$ and can be indexed to a orthorhombic phase (space group $Cmc2_1$) in agreement with JCPDS data (File number 01-080-0656) for spertiniite. Appearance of sharp peaks indicates good crystallinity of the synthesized material. However, a somewhat noisy background in the diffractogram may have originated from the nanocrystalline nature. The calculated lattice parameters are found to be a = 2.953 Å, b = 10.594 Å, and c = 5.277 Å, which are in good agreement with the literature values.[39] No additional peaks could be detected in the diffractogram indicating absence of possible impurity phases such as oxides of copper. However, it is to be noted that the diffractogram for the synthesized GO (Fig.S1, ESI^+) shows two peaks at 2θ values of 25.2° and 42.1°, which can be assigned to reflections from (002) and (100) planes.[40] These peaks overlap with the peaks due to reflections from the (021) and (131) planes of $Cu(OH)_2$. Thus, though the XRD results indicate formation of $Cu(OH)_2$@RGO with good crystallinity, presence of any unreacted GO cannot be ruled out. Therefore, the

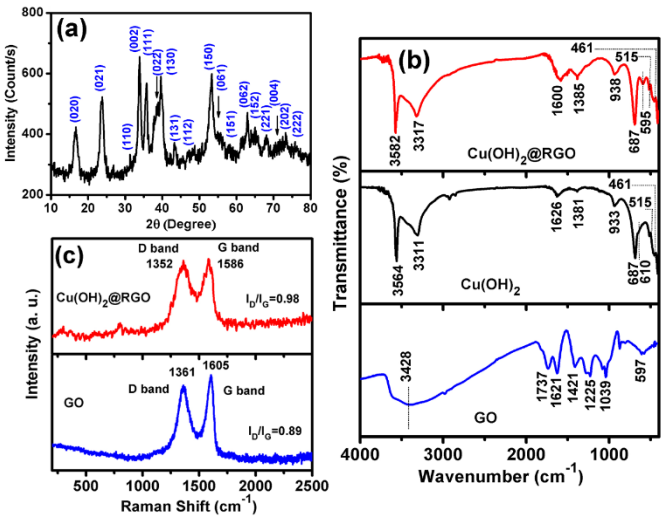

Fig.1 (a) X-ray diffractogram of synthesized $Cu(OH)_2$@RGO (b) FTIR spectra of $Cu(OH)_2$@RGO, $Cu(OH)_2$ and GO, and (c) Raman spectra of $Cu(OH)_2$@RGO and GO.

structural features of the synthesized $Cu(OH)_2$@RGO were further characterized by Fourier transformed infra-red spectroscopy (FTIR) and Raman spectroscopy to ascertain conversion of GO to RGO.

(Fig.1b) shows the FITR spectra of $Cu(OH)_2$, GO and $Cu(OH)_2$@RGO. In $Cu(OH)_2$, presence of peaks at 3564 and 3311 cm^{-1} reflects stretching modes of hydroxyl groups in $Cu(OH)_2$. Similar bands have been observed for $Cu(OH)_2$@RGO at 3582 and 3317 cm^{-1}. The intense nature of these bands is indicative of good crystalline quality.[41] The band at 1628 cm^{-1} reflects the bending mode of the absorbed water in $Cu(OH)_2$ which appears at 1600 cm^{-1} for $Cu(OH)_2$@RGO. On the other hand, C-O stretching vibration at 938 cm^{-1} can be assigned to the corresponding metal cation (Cu^{2+}) in $Cu(OH)_2$@RGO which appears at 933 cm^{-1} for pristine $Cu(OH)_2$.[42-45] The peak at 687 cm^{-1} corresponds to the bending vibration of hydrogen-bounded OH groups. The Cu-O stretching and Cu-O-H bending vibrations occur at lower frequencies and are observed at 595 cm^{-1} for $Cu(OH)_2$@RGO and at 610 cm^{-1} for $Cu(OH)_2$. In the FTIR spectrum for GO, a number of characteristic absorption bands are observed. The band at 3428 cm^{-1} corresponds to the stretching vibrations of O-H, while the bands at 1737, and 1039 cm^{-l} correspond to the stretching vibrations of C=O, and C-O-C, respectively. On the other hand, the bands at 1621, 1421 and 1225 cm^{-l} can be attributed to the vibration of carboxyl groups.[46-47] These bands become weak or disappear completely when GO is reduced to RGO.[48] In the spectrum for $Cu(OH)_2$@RGO, complete disappearance of the peaks at 1737, 1421, 1225 and 1039 cm^{-1} indicates removal of oxygenated groups and appearance of a new peak at 1385 cm^{-1} indicates C-N stretching vibration. Further, presence of a strong C=C stretching peak at 1600 cm^{-1} suggests a restoration of graphite basal plane. Therefore, the FTIR studies clearly indicate complete reduction of GO to RGO forming $Cu(OH)_2$@RGO composite.

Raman spectroscopy is an important tool to characterize carbon containing materials. (Fig.1c) shows Raman spectra of GO and $Cu(OH)_2$@RGO. The Raman spectrum of GO exhibits two noticeable peaks centered at 1605 and 1361 cm^{-1}, which are assigned to the G-band and D-band, respectively.[49] The G-band is linked to the stretching of sp^2-hybridised carbon atoms (E_2g phonons) while the D-band originates from the disordered graphitic carbon indicating presence of defects.[50-51] Therefore, the I_D/I_G ratio is a good measure of the relative concentration of disorder or defect and the average size of the p-conjugation.[49,52] An I_D/I_G ratio of 0.89 has been found for GO. In the Raman spectrum of $Cu(OH)_2$@RGO composite, both the G-band and D-band are found to be shifted to lower frequency region (centered at 1586 and 1352 cm^{-1} respectively) i.e. toward graphitic nature, confirming reduction of GO to RGO.[53, 54] It is expected that the intensity of the D-band will gradually decrease when the GO is reduced. However, a higher I_D/I_G ratio (0.98) for $Cu(OH)_2$@RGO with respect to that for GO suggests an intimate interaction between $Cu(OH)_2$ and RGO resulting in more defects and destruction of sp^2 domains.[55] Viewed from another angle, such kind of interaction would lead to a better charge transfer through defect-assisted propagation during electrochemical processes.

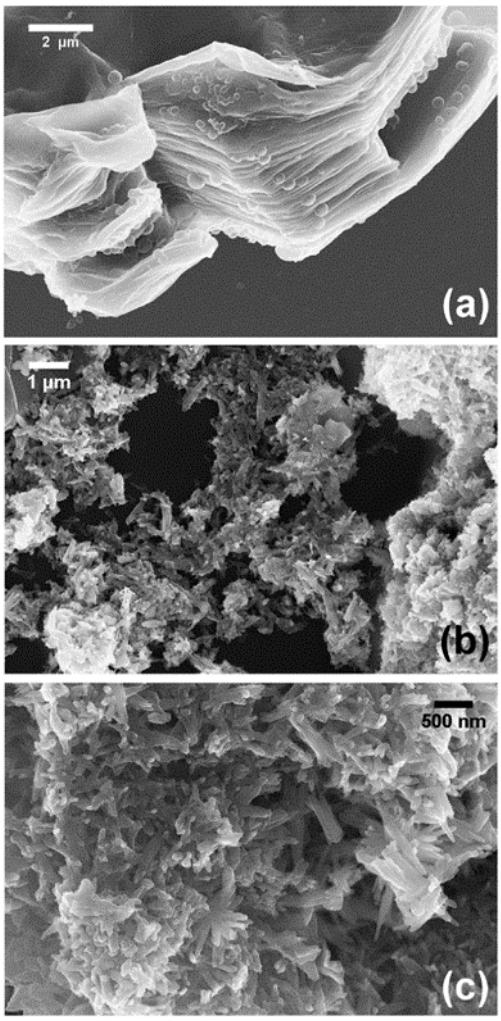

Fig.2 FESEM micrographs of (a) GO (b) $Cu(OH)_2$@RGO at low magnification and (c) $Cu(OH)_2$@RGO at high magnification.

The morphology and microstructure of the synthesized $Cu(OH)_2$@RGO have been investigated by FESEM and TEM. (Fig.2a) shows the FESEM micrograph of GO. The stacked layers of GO sheets, slightly corrugated due to partial exfoliation, are clearly visible. The low and high magnification FESEM images of $Cu(OH)_2$@RGO (Fig.2b & 2c) show that the morphological features consist of uniformly distributed cluster of nanorods, bundled together. TEM images (Fig. 3a and 3b) also reveal that these nanorod bundles are uniformly dispersed in a RGO matrix forming a well interconnected hybrid network and are coated with a thin RGO layer. The average diameter of these nanorods is estimated to be ~12 nm. From the high resolution TEM image, the thickness of the RGO layer has been estimated to be ~6 nm. Well resolved lattice fringes, observed in the HRTEM image (Fig.3c), indicates good crystallinity of the RGO layer with an interplanar spacing of 0.21 nm which corresponds to (107) planes of RGO. For

$Cu(OH)_2$, clear lattice fringes with interplanar spacing of 0.23 nm and 0.25 nm corresponding to (022) and (111) planes could be observed. Observation of well resolved spots arranged in circular rings further confirms formation of orthorhombic $Cu(OH)_2$ with a good crystallinity. Formation of such bundled nanorods could be explained as follows: Cu^{2+} ions have a strong tendency for square planar coordination with OH^- forming extended chains. Interlinking of these chains through coordination of OH to dz^2 of Cu^{2+} would form a two-dimensional (2D) layer structure which, in turn, would stack upon one another through hydrogen bonding.[56] Relative growth rates of different crystal faces determine the final morphology.

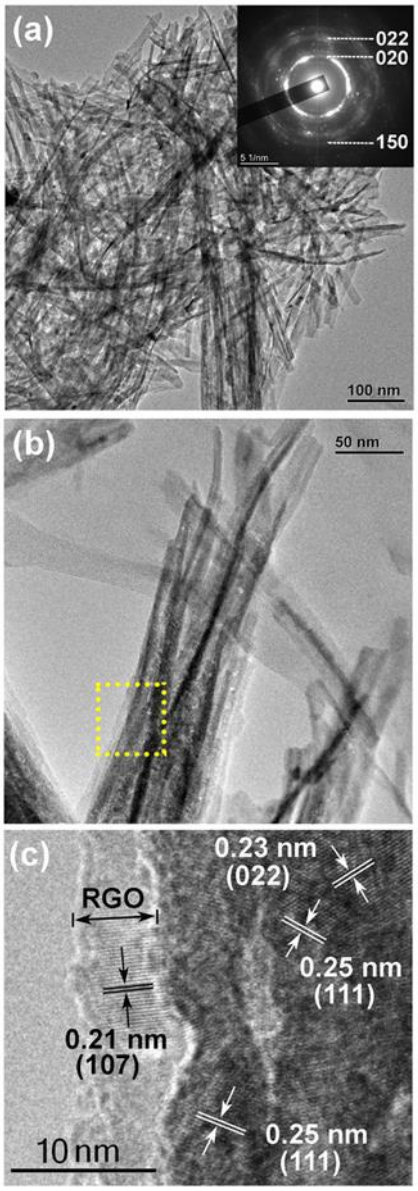

Fig.3 TEM images of synthesized $Cu(OH)_2$@RGO (a) low magnification with the SADP in the inset, (b) high magnification and (c) HRTEM image (taken from the marked area in Fig.3b).

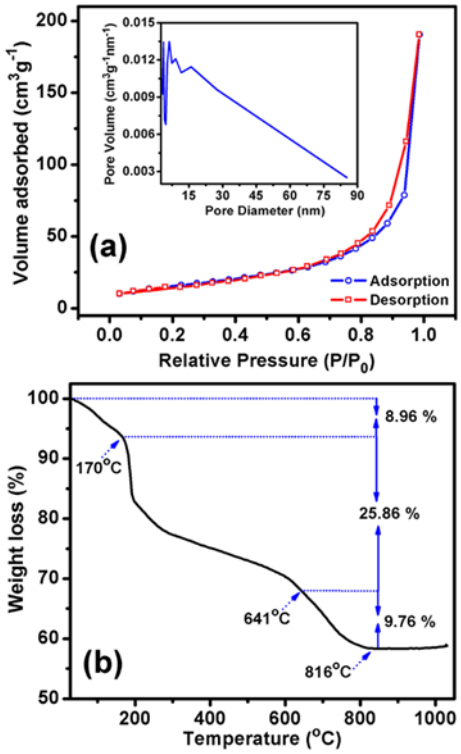

Fig.4 (a) Adsorption desorption isotherms with pore size distribution (inset) and (b) TGA curve of $Cu(OH)_2$@RGO.

During the formation of orthorhombic $Cu(OH)_2$, the growth rate being proportional to $1/d_{hkl}$, growth along [100] far outpaces the growth along other directions resulting in nanorods with a high aspect ratio. Also, as the interlayer H-bonding is weakened in the alkaline condition, the nanorods are bundled in a self-assembled manner due to the interfacial tension.[57]

Dimension of the pores and their distribution are important parameters for a supercapacitor electrode material as these will regulate the access of electrolytes to the interior surfaces. N_2 absorption-desorption isotherms and corresponding pore size distribution plots of the synthesized $Cu(OH)_2$@RGO are shown in (Fig.4a). Convex nature till $P/P_0 = 1.0$ indicates a type III isotherm. The hysteresis loop starts from $P/P_0 = 0.4$ revealing a mixed H3 and H1 type and indicating existence of both inter-particle and structural pores. From the pore size distribution plot, calculated from the adsorption part of the isotherms (inset of Fig.3a) a mesoporous nature is revealed where, the structural pores are indicated by two narrow pore size distributions centered at ~4 and ~6 nm and the inter-particle pores are indicated by a broad pore-size distribution in the range of 10-85 nm. Existence of such kind of mesopores and macropores would allow the interior surfaces to be wetted by the electrolyte and available for electrochemical reactions. A high BET surface area of 78.7 $m^2\ g^{-1}$ has been obtained for $Cu(OH)_2$@RGO with a pore volume of 0.0135 $cm^3\ g^{-1}\ nm^{-1}$.

The thermal stability of the synthesized $Cu(OH)_2$@RGO has been investigated by thermogravimetric analysis. (Fig.4b)

shows the TGA plot at a heating rate of 10°C min^{-1} under constant argon flow. The observed weight losses can be assigned to three major steps: (i) a weight loss of ~8.96% between 30-170°C due to loss of physically absorbed water, (ii) a major weight loss of ~25.86% between 170-641°C due to the decomposition of reduced graphene oxide to CO_2, and (iii) a weight loss of ~9.46% between 641-816°C due to the formation of CuO from $Cu(OH)_2$. Usually, $Cu(OH)_2$-CuO conversion is known to occur at ~892°C,[38] but presence of carbon in the composite may accelerate the process. Therefore, the thermal analysis results indicate that the synthesized $Cu(OH)_2$@RGO is thermally stable up to ~170°C.

3.2 Electrochemical properties

3.2.1 Three electrode cells

The electrochemical properties of $Cu(OH)_2$@RGO were first examined in three-electrode configuration by using a Pt mesh as counter electrode and Ag/AgCl (3 M KCl) as reference electrode. Similar experiments were also carried out on pristine $Cu(OH)_2$ for comparison. (Fig.5a & 5b) show the CV scans in the potential range 0.0-0.47 V with scan rates of 2-100 mV s^{-1} for $Cu(OH)_2$ and $Cu(OH)_2$@RGO respectively. In both cases, the shape of the voltammograms deviates from the ideal rectangular nature indicating predominant pseudocapacitive behaviour.[58] However, increase in the CV area for $Cu(OH)_2$@RGO with respect to $Cu(OH)_2$ indicates that presence of RGO strongly enhances the electrochemical activity of $Cu(OH)_2$. A pair of symmetric redox peaks is observed at ~0.25/0.35 V vs Ag/AgCl (3 M KCl) which can be assigned to reversible Cu(II)/Cu(III) redox reactions involving one electron transfer process:[26]

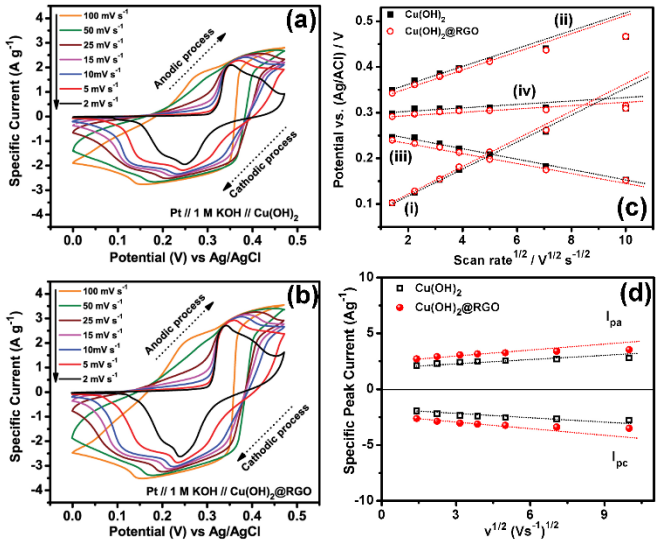

Fig.5 Cyclic voltammograms of (a) $Cu(OH)_2$ and (b) $Cu(OH)_2$@RGO in three-electrode configuration in the potential window of 0.0 to 0.47 V; (c) potential separation (i), variation of anodic and cathodic peak potentials (ii & iii), midpoint potential with square root of scan rate (iv), and (d) Randles-Sevcik plot.

$$Cu(OH)_2 + OH^- \leftrightarrow CuO.OH + H_2O + e^- \qquad (1)$$

In aqueous KOH electrolyte, RGO is known to show pseudo capacitance, besides EDLC, in the potential range of -0.1~-0.3 V vs SCE.[59] Therefore, in the present case, the contribution from RGO is limited to EDLC only. Interestingly, with increasing scan rate, the shape of CV changes and tends to approach a rectangular shape, typical of capacitive behavior. Also, the anodic and cathodic peaks are shifted towards more positive and more negative side respectively indicating that the voltammetric current is diffusion controlled. Such type of shifting of redox peaks are commonly observed for metal hydroxides such as $Ni(OH)_2$,[24-25] and $Co(OH)_2$.[22-23]

The separation potential (ΔE_P) of the cathodic and anodic peaks is a measure of reversibility of the redox processes. A small ΔE_P of 102 mV at a scan rate of 2 mV s^{-1} indicates a good reversibility of electrochemical processes occurring in $Cu(OH)_2$ as given in Eqn.1. As seen from [Fig.5c (i)], no significant difference in ΔE_P is observed between $Cu(OH)_2$@RGO and $Cu(OH)_2$ at each of the scan rates ranging from 2 mV s^{-1} to 100 mV s^{-1} indicating that presence of RGO does not influence the reversibility of the faradic processes of $Cu(OH)_2$. However, as the scan rate increases, ΔE_P increases suggesting a quasi-reversible kinetics which is diffusion controlled. This is further confirmed by observance of a near linear dependence of peak currents on square root of scan rates (Randles-Sevcik plot) as shown in (Fig. 5d). Also, it is observed that the anodic peak potential shifted positively and the catholic peak potential shifted negatively following a linear dependence on $v^{1/2}$ [Fig.5c (ii) & (iii)] and the mid-point potential (formal potential) is found to be independent of the scan rate [Fig.5c (iv)] demonstrating the typical characteristics of redox reactions.[60]

(Fig.6a & 6b) show the galvanostatic charge-discharge (GCD) profiles at different current densities of 0.2-10.0 Ag^{-1} for $Cu(OH)_2$@RGO and $Cu(OH)_2$ respectively. For both cases, as expected, the shapes of charging and discharging curves were not ideal straight lines, confirming the pseudocapacitive behavior. However, a large increase in capacitance is observed at all current densities for $Cu(OH)_2$@RGO compared to $Cu(OH)_2$. This can be assigned to the increased conduction network in RGO enhancing the charge transport. Also, Raman spectroscopy results suggest an intimate interaction between $Cu(OH)_2$ and RGO whereby the sp^2 domains of RGO are partially destructed creating defects which would lead to a better charge transfer through defect-assisted propagation. With increasing current density, the plateau region in the charge curve diminishes supporting the observations in CV.

The specific capacitance (Cs) values have been calculated from GCD using the following equation:

$$\mathbf{Cs} = \frac{\mathbf{I} \times \Delta \mathbf{t}}{\mathbf{m} \times \Delta \mathbf{V}} \qquad (2)$$

where, the m is the total mass of the materials in the electrode excluding the weight of PTFE binder. While in most of the

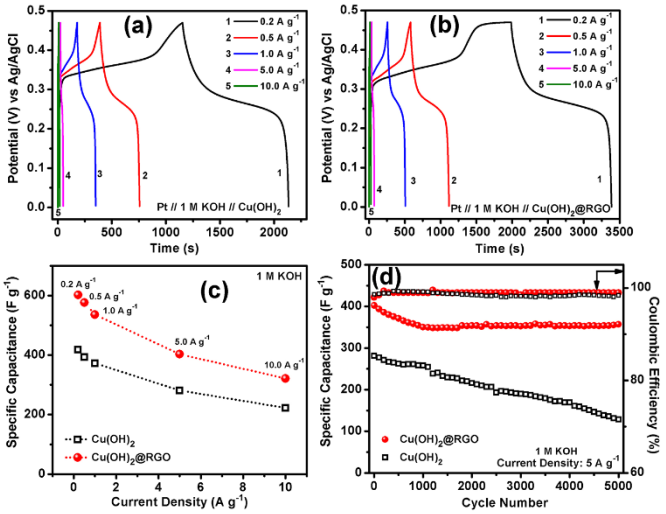

Fig.6 Galvanostatic charge-discharge plots of (a) $Cu(OH)_2$ and (b) $Cu(OH)_2$@RGO in the potential window of 0.0 to 0.47 V at different current densities from 0.2 to 10 A g^{-1}, (c) variation of specific capacitance with increasing current density and (d) cycling performance and columbic efficiency for $Cu(OH)_2$ and $Cu(OH)_2$@RGO in three-electrode cells.

reports the weight of only the active material is used for calculating C_s (leading to a higher value), it is more reasonable to consider the total mass of the electroactive materials as carbon would contribute to the EDLC component. Fig.6c shows the variation of specific capacitance with increasing the current density (0.2–10.0 Ag^{-1}) for both $Cu(OH)_2$@RGO and $Cu(OH)_2$. At a current density of 0.2 Ag^{-1}, a Cs value of 419 Fg^{-1} is observed for $Cu(OH)_2$. This value is only 42% of the theoretical capacitance (989 F g^{-1}) of $Cu(OH)_2$ calculated on the basis of one-electron transfer process. At the same current density, $Cu(OH)_2$@RGO exhibits a much higher Cs value of 602 Fg^{-1} highlighting the positive effect of RGO in enhancing the charge transport. However, in both cases, as the current density is increased, a gradual decrease in Cs is observed. Nonetheless, even at a very high current density of 10 Ag^{-1}, $Cu(OH)_2$@RGO shows a Cs of 322 F g^{-1} compared to only 222 F g^{-1} shown by $Cu(OH)_2$. The observed capacitance values are much higher than the value (120 F g^{-1} at 10 mVs^{-1}) reported previously for $Cu(OH)_2$.[26] Further, the present results are superior to the capacitance obtained for lotus-like $CuO/Cu(OH)_2$ (278 Fg^{-1} at 2 mA cm^{-2}) [61] or RGO/Cu_2O (98.5 Fg^{-1} at 1 Ag^{-1}) .[62]

Prolonged cycle life and ability to deliver power within a very short time are the two essential requirements of a practical supercapacitor. Therefore, cycling performance of $Cu(OH)_2$@RGO has been tested at a high current density of 5 A g^{-1} for 5000 charge-discharge cycles and compared to that of $Cu(OH)_2$ (Fig.6d). Pristine $Cu(OH)_2$ shows a rapid fading in capacitance with increasing cycle number. As a result, only 45.6 % of the first cycle specific capacitance of 128 Fg^{-1} is retained after 5000 cycles. On the other hand, dramatic improvement in the cycling performance is observed for $Cu(OH)_2$@RGO. A much higher specific capacitance of 402 Fg^{-1} is obtained for $Cu(OH)_2$@RGO in the first cycle. After an initial decrease for about 1000 cycles, a steady Cs value of 357 Fg^{-1} is observed till 5000 cycles with no further fading. Also, the coloumbic efficiency approaches unity. Such good cycling stability can be ascribed to the unique 3D nanostructures comprising of bundled nanorods and to the presence of RGO which helps in mitigating the volume expansion of $Cu(OH)_2$ during repeated charging and discharging.

3.2.2 Symmetric cell in two-electrode configuration

While a three-electrode cell provides valuable information about the electrochemical characteristics of a specific material, a two-electrode test cell matches more closely the physical configuration and charge transfer that occurs in a practical supercapacitor although generally with a lower value of specific capacitance.[63] In order to check the practical applicability, the electrochemical properties of the synthesized $Cu(OH)_2$@RGO have been investigated in two-electrode configuration by assembling symmetric $Cu(OH)_2$@RGO//1 M KOH//$Cu(OH)_2$ @RGO coin cells. (Fig.7a) shows the cyclic voltammograms recorded at different scan rates of 2-100 mVs^{-1} in the potential window of -0.9 to 0.9 V. It is noteworthy that by constructing the full cell, the potential window could be extended to 1.8 V. Similar extended voltage of 1.8 V has been observed for two-electrode symmetric Ru//Ru supercapacitor[33] and 1.6 V for symmetric RuO_2//RuO_2 supercapacitor.[34] The CV curves of the full cell exhibit a quasi-rectangular shape indicating pseudocapacitive behaviour. The features of CV remain unchanged even at a high scan rate of 100 mVs^{-1}, indicating highly reversible charge/discharge response and good rate capability of the device. The corresponding charge discharge profiles are shown in (Fig.7b) at different current densities of 0.05 to 5 Ag^{-1} in the potential window of -0.9 to+0.9V. In accordance with the observations in CV, the charge discharge profiles show a non-linear

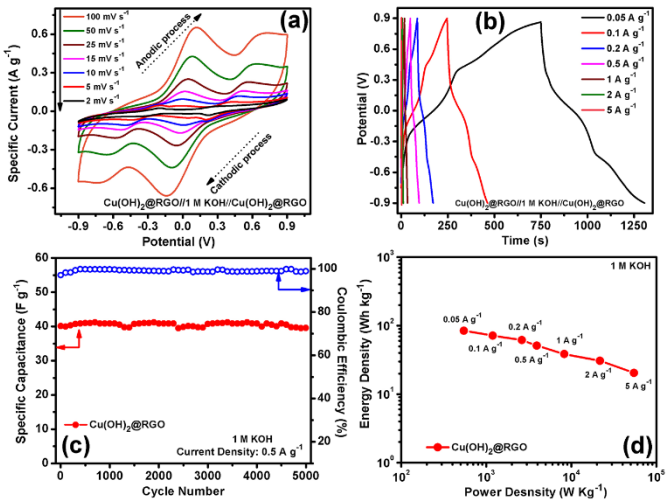

Fig.7 (a) Cyclic voltammograms at different scan rates (2 - 100 mVs^{-1}) in the potential window of -0.9 to 0.9 V, (b) galvanostatic charge-discharge profiles, (c) cycling performance, and (d) Ragone plot of $Cu(OH)_2$@RGO in two-electrode symmetric cell configuration.

behaviour typical of pseudocapacitors. However, as the current density is increased, the profiles tend to become linear. The observed symmetry in the charge and discharge profiles indicates good reversibility. Specific capacitance (Cs) values were calculated from the discharge profile using the equation.[64]

$$Cs = \frac{4 \times I \times \Delta t}{\Delta V \times m} \qquad (3)$$

where, m represents the sum of the total mass of both electrodes excluding the weight of PTFE binder. A high value of 66 Fg^{-1} has been observed at a current density of 0.05 Ag^{-1} (Fig.S2, ESI†). However, with increasing current density the capacitance decreases and at 5 Ag^{-1}, a value of 16 Fg^{-1} is obtained (Fig.S2). The cycling performance of the symmetric cell has been tested at 0.5 Ag^{-1} for 5000 cycles and shown in (Fig.7c). A specific capacitance value of 40 Fg^{-1} is observed in the first cycle. Excellent cycling behavior is observed with no significant decrease in capacitance till 5000 cycles with ~100 % retention. After the few initial cycles, the coulombic efficiency also approaches unity, which has been calculated by using the following equation

$$\eta = \frac{t_D}{t_C} \times 100\% \qquad (4)$$

For a high performance supercapacitor, sustenance of high energy density at high power densities is a key criterion. Energy density and power density values have been calculated from the GCD and the resulting Ragone plots are shown in (Fig.6d). The $Cu(OH)_2$//$Cu(OH)_2$ symmetric cell displays reasonably good values of specific energy and specific power in the range of 84.5-20.5 $WhKg^{-1}$ at 0.55-5.5 $KWKg^{-1}$ along with a relatively slow decrease in energy density with increasing power density. These values are much higher than that of conventional 1.6 V AC//AC symmetric EDLC supercapcitor (10 $WhKg^{-1}$).[65] While there is no prior report available on symmetric $Cu(OH)_2$ cells, there are a couple of recent reports available on 3D highly ordered nanoporous CuO[66] and CuO/graphene[67] where energy density values of 19.7 $WhKg^{-1}$ and 79 $WhKg^{-1}$ have been obtained at power densities of 7000 WKg^{-1} and 565 WKg^{-1} respectively. In comparison, the results obtained in the present work are quite impressive, particularly in terms of power density, which eventually confirm the potential of $Cu(OH)_2$@RGO for high performance energy storage devices.

Conclusions

In summary, a simple one-pot synthesis strategy through low-temperature hydrothermal process is developed to prepare $Cu(OH)_2$@RGO where $Cu(OH)_2$ nanorod bundles embedded in a thin RGO matrix are produced. A high specific capacitance of 602 Fg^{-1} and excellent cycling stability indicate that $Cu(OH)_2$ can be an efficient supercapacitor electrode with superior performance than its oxide counterparts. Such high performance originated from intimate interaction between RGO and $Cu(OH)_2$ and subsequent improved charge transfer through the RGO network, which also serves as a buffering matrix to mitigate volume changes. High BET surface area (78.7 m^2g^{-1}) and mesoporous nature with a broad pore-size distribution, allowing every available surface to be wetted by the electrolyte, also contribute toward achieving high capacitance. The practical applicability of the developed material is demonstrated in two electrode symmetric cells where a high energy density of 84.5 $WhKg^{-1}$ could be achieved together with an excellent power density through retention of an energy density of 20.5 $WhKg^{-1}$ at 54.6 $KWKg^{-1}$.

Acknowledgements

The authors thank Director, CSIR-CGCRI for kind permission to publish this work. Financial support from CSIR via TAPSUN NWP0056 project is gratefully acknowledged.

Notes and references

1 J. Tollefson, *Nature*, 2008, **456**, 436.
2 M. Winter, R. J. Brodd, *Chem. Rev*., 2004, **104**, 4245.
3 E. Frackowiak, F. Béguin, *Carbon*, 2001, **39**, 937.
4 M. Inagaki, H. Konno, O. Tanaike, *J. Power Sources*, 2010, **195**, 7880.
5 L. Wei, G. Yushin, *Nano Energy*, 2012, **1**, 552.
6 M. Kaempgen, C. K. Chan, J. Ma, Y. Cui, G. Gruner, *Nano Lett*., 2009, **9**, 1872.
7 H. Pan, J. Li, Y. P. Feng, *Nanoscale Res Lett.*, 2010, **5**, 654.
8 C. Kim, K.-S. Yang, W.-J. Lee, *Electrochem. Solid-State Lett.*, 2004, **7**, A397.
9 J. Jang, J. Bae, M. Choi, S.-H. Yoon, *Carbon*, 2005, **43**, 2730.
10 Y. Sun, Q. Wu, G. Shi, *Phys. Chem. Chem. Phys.*, 2011, **13**, 17249.
11 M. F. E.-Kady, R. B. Kaner, *Nat. Comm.*, 2013, **4**, 2446.
12 G.A. Snook, P. Kao, A. S. Best, *J. Power Sources*, 2011, **196**, 1.
13 X. Lu, W. Zhang, C. Wang, T.-C. Wen, Y. Wei, *Progress in Polymer Science,* 2011, **36**, 671.
14 S. Maiti, A. Pramanik, S. Mahanty, *ACS Appl. Mater. Interfaces*, 2014, **6**, 10754.
15 J. W. Lee, A. S. Hall, J.-D. Kim, T. E. Mallouk, *Chem. Mater.*, 2012, **24**, 1158.
16 C. Zheng, C. Cao, Z. Ali, J. Hou, *J. Mater. Chem. A*, 2014, **2**, 16467.
17 R. R. Salunkhe, K. Jang, S.-w. Lee, H. Ahn, *RSC Adv.*, 2012, **2**, 3190.
18 H. Chen, L. Hu, M. Chen, Y. Yan, L. Wu, *Adv. Funct. Mater.*, 2014, **24**, 934.
19 T. Zhao, H. Jiang, J. Ma, *J. Power Sources*, 2011, **196**, 860.
20 K. Xie, J. Li, Y. Lai, W. Lu, Z. Zhang, Y. Liu, L. Zhou, H. Huang, *Electrochem. Commun.*, 2011, **13**, 657.
21 X. Zhao, C. Johnston and P. S. Grant, *J. Mater. Chem.*, 2009, **19**, 8755.
22 V. Gupta, S. Gupta, N. Miura, J. Power Sources, 2008, 177, 685.
23 A. D. Jagadale, V. S. Kumbhar, D. S. Dhawale, C. D. Lokhande, *Electrochim. Acta*, 2013, **98**, 32.
24 H. Jiang, T. Zhao, C. Li, J. Ma, *J. Mater. Chem*., 2011, **21**, 3818.
25 M.-S. Wu, K.-C. Huang, *Chem. Commun.*, 2011, **47**, 12122.
26 K.V. Gurav, U.M. Patil, S.W. Shin, G. L. Agawane, M. P. Suryawanshi, S. M. Pawar, P. S. Patil, C. D. Lokhande, J.H. Kim, *J. Alloys Compd.*, 2013, **573**, 27.

27 S. K. Shinde, D. P. Dubal, G. S. Ghodake, P. G.-Romero, S. Kim, V. J. Fulari, *RSC Adv.*, 2015, **5**, 30478.
28 D. P. Dubal, P. Gomez-Romero, B. R. Sankapal, R. Holze, *Nano Energy*, 2015, **11**, 377.
29 K. Chen, S. Song, D. Xue, *CrystEngComm*, 2013, **15**, 144.
30 S. Ko, J. Lee, H. S. Yang, S. Park and U. Jeong, *Adv. Mater.*, 2012, **24**, 4451.
31 W. Kang, F. Liu, Y. Su, D. Wang and Q. Shen, *CrystEngComm*, 2011, **13**, 4174.
32 Y.Z. Long, M.M. Li, C. Gu, M. Wan, J.L. Duvail, Z. Liu, Z. Fan, *Prog. Polym. Sci.*, 2011, **36**, 1415.
33 H. Xia, B. Li, L. Lu, *RSC Adv.*, 2014, **4**, 11111.
34 H. Xia, Y. S. Meng, G. Yuan, C. Cui, L. Lu, *Electrochem. Solid-State Lett.*, 2012, **15**, A60.
35 A. S. Adekunle, K. I. Ozoemena, B. B. Mamba, B. O. Agboola, O. S. Oluwatobi, *Int. J. Electrochem. Sci.*, 2011, **6**, 4760.
36 W. S. Hummers, R. E. Offeman, *J. Am. Chem. Soc.*, 1958, **80**, 1339.
37 S. Sil, N. Kuhar, S. Acharya, S. Umapathy, *Sci. Rep.*, 2013, **3**, 3336.
38 A. Pramanik, S. Maiti, S. Mahanty, *J. Mater. Chem. A*, 2014, **2**, 18515.
39 P. Gao, M. Zhang, Z. Niu and Q. Xiao, *Chem. Commun.*, 2007, 5197.
40 Wang, Y.; Li, Y. M.; Tang, L. H.; Lu, J.; Li, J. H. *Electrochem. Commun.*, 2009, **11**, 889.
41 O. Mabayoje, M. Seredych, T. J. Bandosz, *ACS Appl. Mater. Interfaces*, 2012, **4**, 3316.
42 L. Zhang, W. Lu, Y. Feng, J. Ni, Y. Lü, X. Shang, *Acta Phys. - Chim. Sin.*, 2008, **24**, 2257.
43 K. Nakamoto, Infrared spectra of inorganic and coordination compound. 4th ed. Trans. D. R. Huang, R. Q. Wang, Beijing: Chemical Industry Press, 1991:251.
44 A. Bernson, J. Lindgren, W. Huang, R. Frech, *Polymer*, 1995, **36**, 4471.
45 J. M. Aguirre, A. Gutierrezb and O. Giraldo, *J. Braz. Chem. Soc.*, 2011, **22**, 546.
46 B. Das, K. E. Prasad, U. Ramamurty, C. N. R. Rao, *Nanotechnology*, 2009, **20**, 125705.
47 H. Hu, X. Wang, F. Liu, J. Wang, C. Xu, *Synth. Met.*, 2011, **161**, 404.
48 Q. Chen, L. Zhang, G. Chen, *Anal. Chem.*, 2012, **84**, 171.
49 C.H. Xu, J. Sun, L. Gao, *J. Mater. Chem.*, 2012, **22**, 975.
50 D Graf, F. Molitor, K. Ensslin, C. Stampfer, A. Jungen, C. Hierold, L. Wirtz, *Nano Lett.*, 2007, **7**, 238.
51 A. C.Ferrari, J. C. Meyer, V. Scardaci, C. Casiraghi, M. Lazzeri, F. Mauri, S. Piscanec, D. Jiang, K. S. Novoselov, S. Roth, A. K. Geim, *Phys. Rev. Lett.*, 2006, **97**, 187401.
52 Y. Ye, P. Wang, E. Dai, J. Liu, Z. Tian, C. Liang, G. Shao, *Phys. Chem. Chem. Phys.*, 2014, **16**, 8801.
53 K. N. Kudin, B. Ozbas, H. C. Schniepp, R. K. Prud'homme, I. A. Aksay, R. Car, *Nano Lett.*, 2008, **8**, 36.
54 T. S. Sreeprasad, A. K. Samal, T. Pradeep, *J. Phys. Chem. C*, 2009, **113**, 1727.
55 Y. Yang, L. Ren, C. Zhang, S. Huang, T. Liu, *ACS Appl. Mater. Interfaces*, 2011, **3**, 2779.
56 Z. R. Dai, Z. L. Wang, *Nano Lett.*, 2002, **2**, 1397.
57 W. Zhang, X. Wen, S. Yang, Y. Berta, L. Wang, *Adv. Mater.*, 2003, **15**, 822.
58 S. Maiti, A. Pramanik, S. Mahanty, *Chem. Commun.*, 2014, **50**, 11717.
59 W. Si, X. Wu, J. Zhou, F. Guo, S. Zhuo, H. Cui, W. Xing, *Nanoscale Res. Lett.,* 2013, **8**, 247.
60 J. Yang, S. Gunasekaran, *Carbon*, 2013, **51**, 36.
61 Y.-K. Hsu, Y.-C. Chen, Y.-G. Lin, *J. Electroanal. Chem.*, 2012, **673**, 43.
62 X. Dong, K. Wanga, C. Zhao, X. Qian, S. Chen, Z. Li, H. Liu, S. Dou, *J. Alloys Compd.*, 2014, **586**, 745.
63 M. D. Stoller, R. S. Ruoff, *Energy Environ. Sci.*, 2010, **3**, 1294.
64 M. Ghaffari, Y. Zhou, H. Xu, M. Lin, T. Y. Kim, R. S. Ruoff, Q. M. Zhang, *Adv. Mater.*, 2013, **25**, 4879.
65 B. Xu, F. Wu, R. Chen, G. Cao, S. Chen, G. Wang, Y. Yang, *J. Power Sources*, 2006, **158**, 773.
66 S. E. Moosavifard, M. F. E.-Kady, M. S. Rahmanifar, R. B. Kaner, M. F. Mousavi, *ACS Appl. Mater. Interfaces*, 2015, **7**, 4851.
67 A. Pendashteha, M. F. Mousavia, M. S. Rahmanifar, *Electrochim. Acta*, 2013, **88**, 347.

Table of Contents Entry

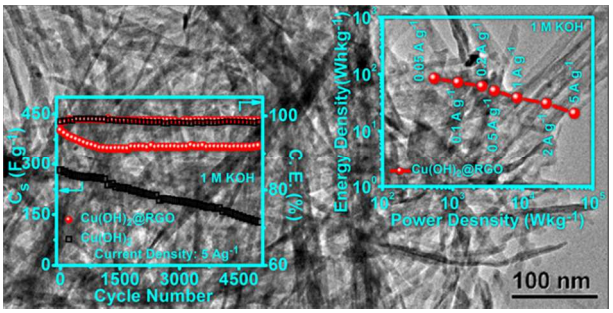

$Cu(OH)_2$@RGO symmetric supercapacitor cell shows excellent energy density and power density (84.5 W h Kg^{-1} at 550 W Kg^{-1})